Winds of Change: Scope, causes and implications of a reversal in global terrestrial stilling for wind energy

Increasing global terrestrial winds are increasing wind energy

Zhenzhong Zeng[1,*], Alan D. Ziegler[2], Timothy Searchinger[3], Long Yang[1], Anping Chen[4], Kunlu Ju[5], Shilong Piao[6], Laurent Z. X. Li[7], Philippe Ciais[8], Junguo Liu[9], Deliang Chen[10], Cesar Azorin-Molina[10,11], AdrianChappell[12], David Medvigy[13], Eric F. Wood[1]

[1] Department of Civil and Environmental Engineering, Princeton University, Princeton, New Jersey 08544, USA (include your new affiliation)

[2] Geography Department, National University of Singapore, 1 Arts Link Kent Ridge, Singapore 117570, Singapore

[3] Woodrow Wilson School, Princeton University, Princeton, New Jersey 08544, USA

[4] Forestry and Natural Resources, Purdue University, West Lafayette, Indiana 47907, USA

[5] School of Economics and Management, Tsinghua University, Beijing 100084, China

[6] Sino-French Institute for Earth System Science, College of Urban and Environmental Sciences, Peking University, Beijing 100871, China

[7] Laboratoire de Météorologie Dynamique, Centre National de la Recherche Scientifique, Sorbonne Université, 75252 Paris, France

[8] Laboratoire des Sciences du Climat et de l'Environnement, UMR 1572 CEA-CNRSUVSQ, 91191 Gif-sur-Yvette, France

[9] School of Environmental Science and Engineering, South University of Science and Technology of China, Shenzhen 518055, China

[10] Regional Climate Group, Department of Earth Sciences, University of Gothenburg, Gothenburg, Sweden

[11] Centro de Investigaciones sobre Desertificación, Consejo Superior de Investigaciones Cientificas (CIDE-CSIC), Montcada, Valencia, Spain

[12] School of Earth and Ocean Sciences, Cardiff University, Wales, CF10 3AT, UK

[13] Department of Biological Sciences, University of Notre Dame, Notre Dame, IN 46556, USA

*Correspondence to: zzeng@princeton.edu

Manuscript for *Nature Climate Change*

June 20, 2019

Wind power is a rapidly growing alternative energy source to achieve the goal of the Paris Agreement under the United Nations Framework Convention on Climate Change, to keep warming well below 2 ◦C by the end of the 21st century. Widely reported reductions in global average surface wind speed since the 1980s, known as terrestrial stilling, however, have gone unexplained and have been considered a threat to global wind power production. Our new analysis of wind data from *in-situ* stations worldwide now shows that terrestrial stilling reversed around 2010 and global wind speeds over land have recovered most of the losses since the 1980s. Concomitant increased surface roughness from forest growth and urbanization cannot explain prior stilling. Instead we show decadal-scale variations of near-surface wind are very / quite likely caused by the natural, internal decadal ocean/atmosphere oscillations of the Earth's climate system. The wind strengthening has increased the amount of wind energy entering turbines by 17 ±2% for 2010-2017, likely increasing U.S. wind power capacity by 2.5%. The increase in global terrestrial wind bodes well for the immediate future of wind energy production in these regions as an alternative to fossil fuel consumption. Projecting future wind speeds using ocean/atmosphere oscillations show wind turbines could be optimized for expected wind speeds, including small and large speeds, during the productive life spans of the turbines.

Reports of a 8% global decline in land surface wind speed (~1980 to 2010) have raised concerns about output from future wind power[1-5]. Wind power varies with the cube of wind speed (u) [6]. The decline in wind speed is evident in the northern mid-latitude countries where the majority of wind turbines are installed including China, the U.S. and Europe[1]. If the observed 1980-2010 decline in wind speed continued until the end of the century, global u would reduce by 21%, halving the amount of power available in the wind. Understanding the drivers of this long-term decline in wind

speed is critical not merely to maximize wind energy production[9-11] but also to address other globally significant environmental problems related to stilling, including reduced aerosol dispersal, reduced evapotranspiration rates, and adverse effects on animal behavior and ecosystem functioning[1,3,4,12].

The potential causes for the global terrestrial stilling are complex and remain contested (e.g., Vautard et al., 2010; McVicar et al., 2012; Torralba et al., 2017; Wu et al., 2018). Terrestrial surface winds are driven by atmosphere circulations and momentum extracted by rough land surface. Many regional-scale studies using reanalysis datasets have found correlations of *u* to some climate indices (e.g., Chen and Pryor, 2013; Nchaba et al., 2017; Naizghi and Quarda, 2017; Azorin-Molina et al., 2018). Those studies hypothesize that the terrestrial stilling is caused by decreased driving force due to the change in large scale circulations (Torralba et al., 2017). The hypothesis is supported by the consistency between the wind speed changes at the surface and at higher levels in the reanalysis datasets (Refs???) Consistent wind speed change cannot be explained by change in land surface (Chen and Pryor, 2013; Torralba et al., 2017). However, there are no feedbacks between land surface change, aerodynamic roughness and wind speed i.e., wind speed reanalysis data does not represent land surface dynamics. There are large uncertainties in the reanalysis datasets (e.g., Vautard et al., 2010; Chen and Pryor, 2013; Torralba et al., 2017) and, more importantly, the global terrestrial stilling is either not reproduced or has been largely underestimated in global reanalysis products[2,8] (Supplementary Fig. 1) or climate model simulations for IPCC AR5 (Supplementary Fig. 2). The discrepancies between the decreasing trends derived from *in situ* stations and from reanalysis or climate model simulations lead to an alternative hypothesis. Global terrestrial stilling is caused by increased drag from increased land

surface roughness from global 'greening' of the Earth and/or urbanization[2,7], both of which would suggest further future declines.

Recent studies have described wind speed reversal at local scales[16,17] (Tobin et al. 2014, Kim and Paik 2015) or in annual climate reports at global scale[18] (Tobin et al. 2014). However, there is no clear global trend of wind speed change (e.g. refs 5, 8). A wind reversal could elucidate the causes of global terrestrial stilling and potentially improve our future wind energy projections. We investigated changes in recent global wind speeds and revealed three key findings: (1) global stilling reversed ~2009-2011 and recovered most of the wind speed over land lost between 1980 and 2010; (2) a strong correlation (r value and p-value?) between global and regional wind speeds over land and decadal changes in global ocean/atmosphere oscillations; (3) recovered terrestrial wind speed explains much of the increase in U.S. wind power capacity over the last decade. These recent phases of the ocean/atmosphere oscillations are likely to continue for at least another decade (references 22,24,25,27,35). Consequently, these changes are promising for future wind power generation in that time period. However, our findings also suggest that wind power output is very (or how much) likely to fluctuate over decadal timescales, which will require appropriate planning of wind turbines.

Our analysis of global land surface wind speed change integrates direct *in situ* observations of *u* from terrestrial weather stations from 1978 to 2017 together with statistical models for detection of trends. The XXXX stations used were selected carefullyfrom a total of 28,149 stations in the Global Summary of Day (GSOD) database following strict quality control procedures (Supplementary Fig. 3; see *Methods* for details). They are mainly distributed in the northern mid-

latitudes countries, including nine of the top 10 cumulative wind power capacity countries: China, USA, Germany, India, Spain, UK, France, Canada, and Italy[13]. As one of our goals is to test for a continuation of the terrestrial stilling after 2010 (refs 1-3), we use a piecewise linear regression model to examine the potential trend changes[14,15].

Extent reversal in global terrestrial stilling

Our analysis shows that global mean annual *u* decreased significantly at a rate of -0.08 m s^{-1} (or -2.3%) per decade during the first three decades beginning in 1978 (P-value < 0.001; Fig. 1a, Supplementary Table 1). The decreasing trend echoes results of prior studies[2-4] and confirms global terrestrial stilling as an established phenomenon during the period of 1978-2010. However, *u* has significantly increased in the current decade. This turning point is statistically significant at P < 0.001 with a goodness of fit of an R^2 = 90% (Fig. 1a). The recent increasing rate of +0.24 m s^{-1} $decade^{-1}$ (P < 0.001) is three times that of the decreasing rate, before the turning point in 2010. Below (where?) Next? we provide robust and comprehensive evidence that the reversal is global and changing at the decadal scale and is not associated with regional events or occurring at random.

To exclude the possibility that the turning point is caused by large wind speed changes at only a few sites, we repeat our analyses 300 times by randomly resampling 40% of the global stations each time (grey lines in Fig. 1a; 40% of the stations are selected to ensure a sufficient sample size (n > 500)). We find significant turning points in each randomly-selected sub-sample (P < 0.001; $R^2 \geq 76\%$). Run-specific turning points occur between 2002 and 2011, with most (95%) of them between 2009 and 2011 (Fig. 1b). In addition, mean annual *u* changes before and after a specific turning point based on the 300 sub-sample estimates are -0.08 ± 0.01 m s^{-1} per decade and 0.24 ±

126 0.03 m s^{-1} per decade, respectively (Fig. 1c), identical to those values based on all the global
127 samples.
128
129 Spatial analyses further confirm that the recent reversal is a global-scale phenomenon
130 (Supplementary Fig. 4a-c). A majority (79%) of the stations where *u* decreased significantly during
131 1978-2010 (Supplementary Fig. 4b) have positive trends in *u* after 2010 (Supplementary Fig. 4c).
132 The stations are mainly distributed over three regions: North America (USA and Canada), Europe
133 (Germany, Spain, United Kingdom, France and Italy), and Asia (mainly China and India).
134 Significant turning points exist in all of the regions mean annual *u* time series ($P < 0.001$,
135 Supplementary Fig. 4d-f), but they vary in the specific year of occurrence. For example, a turning
136 point occurs earlier in Asia (2001, R^2 =80%, Supplementary Fig. 4f) and Europe (2003, R^2 = 56%,
137 Supplementary Fig. 4e) than in North America (2012, R^2 = 80%, Supplementary Fig. 4d).
138 Nevertheless, all regions show a significant increase in *u* after ~2010 (Supplementary Fig. 4d-f).
139
140 The existence of turning points is robust regardless of month (Supplementary Table 1 and
141 Supplementary Fig. 5) or wind variable chosen for analysis (Supplementary Fig. 6), and shows no
142 dependence on quality control procedures for weather station data (Supplementary Fig. 7).
143 Furthermore, we show that our findings are robust and repeatable (Supplementary Fig. 8) using a
144 different data set—the HadISD database. The HadISD database passes similar stringent station
145 selection criteria and quality control tests established by Met Office Hadley Centre[19]. In both
146 datasets??? we find that the tendency for an increasing number of stations becoming automated
147 during recent decades (Supplementary Figs 9 and 10) does not affect the result (Supplementary
148 Fig. 11). To test the effect of inhomogeneity, we remove all the stations with change point as

detected by the Pettit test (Pettitt, 1979), repeat the analyses and find the results have not changed (Supplementary Fig. 12). All these lines of evidence supports our finding that the trends in *u* are not caused by changes in measurement or other systematic errors in the measurement network.

Causes of the reversal in global terrestrial stilling

Next we explore causes of decadal changes in *u* over land. To explain the early global stilling, researchers have offered a variety of theories, many of which are focused on the drag force of *u* linked to terrestrial roughness including urbanization and vegetation changes[2]. These theories have been disputed[20] (also see Supplementary Figs 13 and 14). However, we find that global stilling changed abruptly after 2010which is inconsistent with typically slow change in terrestrial roughness. The variation in *u* (including prior stilling and the recent reversal) is most likely caused by driving forces associated with decadal variability of large-scale ocean/atmospheric circulations. An extensive literature describes change in ocean/atmosphere oscillations, cause adjustments in global circulation, generate stationary atmospheric waves, and lead to massive reorganizations of *u* patterns[21-25] (Chen and Pryor, 2013; Kim and Paik, 2015; Nchaba et al., 2017; Naizghi and Quarda, 2017; Azorin-Molina et al., 2018). The relationship between these oscillations and long-term wind speeds over the entire globe has not been well established.

We investigate whether decadal ocean/atmosphere oscillations can explain these decadal changes in *u* over land. Essentially, wind is physically caused by the uneven heating of the Earth surface (temperature anomalies or heterogeneity), and the latter is widely decscribed by climate indices for oscillations (see *Methods*). To test such associations, we use 21 indicators of ocean/atmosphere oscillations which are well-known and provide information about the decadal variations of

ocean/atmospheric circulations (see description in Supplementary Table 2). These indices are characterized with the observed regional sea surface temperature and pressure anomalies (*Methods*). Second, to avoid overfitting with multiple indices, we apply stepwise regression[26] to identify the six largest explanatory power factors for the decadal variations of u over regions of the globe, North America, Europe, and Asia, respectively (results in Supplementary Table 3). Multiple regression of these six indices (Supplementary Table 3) reconstruct decadal variations of u over the globe with an R^2 of 70 ±5% (79 ±2% for North America, 48 ±9% for Europe, and 51 ±8% for Asia; Supplementary Fig. 15).

To ensure that the correlations are not due to the trend in these data, we detrended all the time series and repeated the stepwise regression analysis. The goodness of fit decreased because the correlation related to the long-term stilling has been largely removed after detrending (Supplementary Fig. 16). However, these detrended indices still significantly and substantially explain the detrended variation of u, particularly for the recent rapid reversal (Supplementary Fig. 16). Furthermore, we train our models only using the detrended time series before the turning points (2010 for the globe, 2012 for North America, 2003 for Europe, and 2001 for Asia), and find that the models are capable to reproduce well the positive trends after the turning points for the globe ($P < 0.001$; Fig. 2a), and all three regions ($P < 0.001$; Fig. 2b-d). The magnitude of the increasing rate after the turning points is well modelled (Fig. 2). These results demonstrate that the ocean/atmosphere oscillations are the key drivers for the recent, rapid reversal of the terrestrial stilling.

The greatest explanatory power factor for each region is associated with the following indices: Tropical Northern Atlantic Index (TNA) for North America ($R = -0.67$, $P < 0.001$); North Atlantic Oscillation (NAO) for Europe ($R = 0.37$, $P < 0.05$); and Pacific Decadal Oscillation (PDO) for Asia ($R = 0.50$, $P < 0.01$) (Supplementary Tables 2 and 3). These three indices are also significantly correlated to global mean annual *u* ($P < 0.01$; Supplementary Table 2). Furthermore, we conducted Granger causality tests, in which we select lag length using a Bayesian information criterion (Granger, 1969). Gobal mean annual *u* is Granger caused by TNA ($P < 0.001$), NAO ($P < 0.01$) and PDO ($P < 0.1$). Regionally, the tests also reject the null hypothesis that TNA does not Granger cause *u* over North America ($P < 0.001$), NAO does not Granger cause *u* over Europe ($P < 0.1$), and PDO does not Granger cause *u* over Asia ($P = 0.11$). Besides, although the reversals of the wind stilling phenomenon in different regions are driven by different climate indices, owing to the ocean/atmosphere oscillations having some degree of synchronization during turning points of multidecadal climate variability (Tsonis et al., 2007; Henriksson, 2018), a global pattern of terrestrial stilling and its reversal emerges (Figs 1 and 2).

To further uncover the mechanisms behind the decadal variations of *u*, we construct the composite annual mean surface temperature for the years that exhibit negative (Fig. 3a) and positive (Fig. 3b) anomalies of detrended *u*. Distinct temperature patterns correspond to both negative and positive *u* anomalies, but exhibits different spatial patterns across the globe. During the years of negative *u* anomalies (Fig. 3a) the following are observed: (a) positive anomalies of temperature prevail over Tropical Northern Atlantic (TNA region, 5.5^{o}N to 23.5^{o}N, 15^{o}W to 57.5^{o}W), showing a positive value for TNA; (b) the west (east) Pacific is warmer (colder) than normal years, demonstrating a negative value for PDO; (c) positive anomalies of temperature occur near the Azores and negative

anomalies occur over Greenland, indicating a negative value for NAO. The opposite pattern (i.e. negative TNA, positive PDO and NAO) occurs during the years of positive *u* anomalies (Fig. 3b). The ocean/atmosphere oscillations, characterized as the decadal variations in these climate indices (mainly TNA, NAO, PDO), can therefore explain the decadal variation of *u* (the long-term stilling and the recent reversal) (Figs 2 and 3f-h).

The PDO and TNA are important predictors regardless of subset of stations used. Yet, while NAO has the largest explanatory power for regional *u* over Europe, there are 169/300 cases that NAO is not included as a major predictor (Supplementary Table 3). Thus, even within Europe, the impact of NAO differs regionally. We thus investigate the spatial patterns of the correlation between the three indices (PDO, TNA, NAO) and the regional ($5^o \times 5^o$) winds (Fig. 3c-e). The regional wind is calculated using all stations within a $5^o \times 5^o$ cell; and only the cells with more than 3 stations are included in the analysis. TNA has a strong, significant negative correlation with regional *u* in North America excluding western Canada and areas near Mexico (Fig. 3c). PDO has a significant positive correlation with regional *u* globally (Fig. 3e). NAO has overwhelmingly significant positive correlation with regional *u* in the United States and Northern Europe, in particular United Kingdom, but negative correlation with regional *u* in Southern Europe (Fig. 3d). Statistically, NAO is significantly and negatively correlated with European winds south of 48^oN ($R = -0.39$, $P < 0.05$), while significantly and positively correlated with European winds north to 48^oN ($R = 0.48$, $P < 0.01$).

There are some theories for the physical mechanisms how the changes in these indices (e.g. TNA, PDO, and NAO) impact on the regional *u* over land[22,24,25,27]. With respect to TNA, previous studies

demonstrate that the positive phase of TNA is linked with a weakened Hadley circulation[24]. We also find that during the positive phase of TNA there is a cold anomaly over the eastern coast of the United States (Fig. 3a) (in line with the finding in ref. 24), which leads to a southward component of surface wind and facilitates a stable environment of weak convergence from tropics to the mid-latitude region. Both the effects indicate that a positive TNA will reduce *u* in the mid-latitudes, the United States in particular (Fig. 3c and Supplementary Fig. 17a,b). As for NAO, the negative and positive phases of NAO have different Jet Stream configurations and wind systems in Northern versus Southern Europe (Supplementary Fig. 17c,d; refer the theory to ref. 22). During the positive phase, a large pressure gradient across the North Atlantic[22] generates strong winds and storms across North America (especially the east coast of the United States) and Northern Europe (Supplementary Fig. 17d). Meanwhile, during its negative phase, a small pressure gradient[22] produces a weakened jet stream across North America and Southern Europe, yet increases storms in Southern Europe (Supplementary Fig. 17c). This theory explains the contrasting correlations of NAO to *u* in northern and southern Europe (Fig. 3d, Supplementary Fig. 18). For PDO, the temperature gradient during the negative (positive) phase generates an easterly (westerly) component of surface wind[25,27], which weakens (strengthens) the prevailing westerly winds in the mid-latitudes (Supplementary Fig. 17e,f). It explains the widespread and significant positive correlations between PDO and *u* across the whole mid-latitudes (Fig. 3e).

Last but not least, it is critical to figure out why global reanalysis products do not reproduce or largely underestimate the historical terrestrial stilling (Supplementary Fig. 1), which is a major basis for the previous studies rejecting the ocean/atmosphere oscillations as a dominant driver for the global terrestrial stilling (e.g. Vartard et al., 2010; Wu et al., 2018). Global reanalysis products

have only assimilated sea level pressure data, and thus the capacities of these products in reproducing surface wind speed over land are determined by Global Climate Model (GCM) used in the assimilation systems. Surface process parameterization schemes (e.g. Monin-Obukhov similarity theory) are used to simulate the winds over land in these models, yet these schemes have uncertainties. We find that in the regions where AMIP simulations (i.e. GCM simulations forcing with the observed SST) capture the stilling, such as Europe and India (Fig. 4a,b in Zeng et al., 2018), the global reanalysis products are also capable to reproduce the stilling in these regions (Fig. S1c); while in the regions where AMIP simulations do not capture the stilling, such as North America (Pryor et al., 2009; Zeng et al., 2018), the global reanalysis products fail to reproduce the stilling (Vautard et al., 2010; Torralba et al., 2017) (Fig. S1b). Therefore, it is the model limitations that make global reanalysis products difficult reproducing the observed wind speed changes in some regions. More efforts are required to improve surface process parameterization scheme and its connection to ocean/atmosphere circulations in the climate models.

Implications for wind energy of the reversal in global terrestrial stilling

Finally, we explore some implications of these changes for the global wind power industry. In wind power assessments, near-surface wind observations from weather stations (u at the height of z_r = 10 meters) are often used to estimate wind speeds at the height of a turbine (u_{tb} at the height of z_{tb} = 50-150 meters) using an exponential wind profile power law relationship:

$$u_{tb} = u\left(\frac{z_{tb}}{z_r}\right)^{\alpha} \quad (2)$$

where the α is commonly assumed to be constant (1/7) in wind resource assessments because the differences between these two levels are unlikely great enough to introduce considerable errors in the estimates (e.g. refs 5, 28-30).

Changes in wind speed matter not only on average but also in the percentage of time wind speeds are high or low. A $u > 3$ m s^{-1} is a typical minimum u needed to drive turbines, so wind speeds below 3 m s^{-1} are typically wasted from a power perspective. Although periods of high wind speed greatly increase the physical capacity to generate power according to formula (1), turbines are built with a maximum capacity, so periods of high wind speed can also "waste" the uses of wind with the threshold depending on the capacity of the turbine.

On average, the increase of global mean annual u from 3.13 m s^{-1} in 2010 to 3.30 m s^{-1} in 2017 (Fig. 1a; see *Methods* for details) increases the amount of energy entering a hypothetical wind turbine receiving the global average wind by 17 ±2% (uncertainty is associated with subsamples in Fig. 1a; regionally, 22 ±2% for North America, 22 ±4% for Europe, and 11 ±4% for Asia). At the hourly scale, we also find that the frequency of low u (<3 m s^{-1}) decreases while the frequency of high u increases (Fig. 4a). Using one General Electric GE 2.5 – 120 turbine[31] (Supplementary Fig. 19) to illustrate, the effects of changes in global average u increase potential power generation from 2.4 million kWh in 2010 to 2.8 million kWh in 2017 (+17%). If present trend persists for at least another decade, in the light of the robust increasing rate during 2000-2017 (Fig. 1a) and the long cycles of natural ocean/atmosphere oscillations[22,24,25,27,35] (Supplementary Fig. 20), power would rise to 3.3 million kWh in 2024 (+37%), resulting in a +3% per decade increase of global-average capacity factor (mean power generated divided by rated peak power) on average. This

change is even larger than the projected change in wind power potential caused by climate change under multi-scenairos (Tobin et al., 2015, 2016).

During the past decade, the capacity factor of the U.S. wind fleet[32] has steadily risen at a rate of +7% per decade (Fig. 4b), which previous reports have attributed solely to technology innovations[33]. We find that the capacity factor for wind generation in the U.S. is highly and significantly correlated with the variation in the cube of regional-average u (u^3, $R = 0.86$, $P < 0.01$; Fig. 4b). To isolate the u-induced increase in capacity factor from that due to technology innovation, we use the regional mean hourly wind speed in 2010 and 2017 to estimate the increase of capacity factor for a given turbine, thereby controlling for technology innovation. It turns out that the increased u^3 explains ~50% of the increase of the capacity factor (see *Methods* for details). Therefore, in addition to technology innovation, the strengthening u is another key factor powering the increasing reliability of wind power in the U.S. (and other mid-latitude countries where u is increasing, such as China and Europe countries).

To illustrate the consequences, one turbine (General Electric GE 1.85 – 87 (ref. 34)) installed at one of our *in-situ* weather stations in the U.S. in 2014 (inset plot in Fig. 4c), which was expected to produce 1.8 ±0.1 million kWh using four years of u records before the installation (2009-2013)[34], actually produced 2.2 ±0.1 million kWh between 2014-2017 (+25%). This system has the potential to generate 2.8 ±0.1 million kWh (+56%) if u recovers to the 1980s level (red bars in Fig. 4d; see *Methods* for details). Globally, 90% of the global cumulative wind capacity has been installed in the last decade[13], during which global u has been increasing (see above).

Discussion

Although the response of ocean/atmosphere oscillations to greenhouse warming remains unclear[27], because these oscillations change over decadal time frames[22,24,25,27,35], the increases in wind speeds should continue for at least a decade. Climate model simulations constrained with historical sea surface temperature also show a long cycle in *u* over land (Supplementary Fig. 20). Our findings are therefore good news for the power industry for the near future.

However, oscillation patterns in the future will likely cause returns to declining wind speeds, and anticipating these changes should be important for the wind power industry. Wind farms should be constructed in the areas with stable winds and high effective utilization hours (e.g. 3 - 25 m s^{-1}). If high wind speeds are likely to be common, building turbines with larger capacities will often be justified. For example, capturing more available wind energy (blue bars in Fig. 4d) could be achieved through the installation of higher capacity wind turbines (e.g. General Electric GE 2.5 – 120, green bars in Fig. 4d), greatly increasing total power generation. Most turbines tend to require replacement after 12-15 years[36]. Further refinement of the relationships uncovered in this paper could allow choices of turbine capacity, rotor and tower that are optimized not just to wind speeds of the recent past but to likely future changes during the lifespan of the turbines.

In summary, we find that after several decades of global terrestrial stilling, wind speed has rebounded, increasing rapidly in the recent decade globally since 2010. Ocean/atmosphere oscillations, rather than increased surface roughness, are likely the causes. These findings are important for those vested in maximizing the potential of wind as an alternative energy source. The development of large-scale alternative energy sources such as wind power[6,9-11,13] is one of the

most effective approaches to reduce anthropogenic gas emissions[10] for the goal to keep warming well below 2 ◦C by the end of the 21st century. One megawatt (MW) of wind power reduces 1,309 tonnes of CO_2 emissions and also saves 2,000 liters of water compared with other energy sources[11,13]. Since its debut in the 1980s, the total global wind power capacity reached 539 gigawatts by the end of 2017, and the wind power industry is still booming globally. For instance, the total wind power capacity in the U.S. alone is projected to increase fourfold by 2050 (ref. 11). The reversal in global terrestrial stilling bodes well for the expansion of large-scale and efficient wind power generation systems in these mid-latitude countries in the near future.

Methods

Wind datasets. The key data used in this analysis is the Global Surface Summary of the Day (GSOD) database processed by the National Climatic Data Center (NCDC) of the United States (download August 1st 2018 from ftp://ftp.ncdc.noaa.gov/pub/data/gsod). The database is derived from the United States Air Force (USAF) DATSAV3 Surface data and the Federal Climate Complex Integrated Surface Hourly dataset, which is grounded on data exchanged under the World Meteorological Organization (WMO) World Weather Watch Program according to WMO Resolution 40 (Cg-XII)[39]. There is a total of 28,149 stations included in the GSOD database globally (for the distributions see the dots in Supplementary Fig. 3). Online data are available from 1929 to the present, with data for the past four decades being the most complete. Daily data for each station include mean wind speed, maximum sustained wind speed, maximum wind gust, mean temperature, maximum temperature, minimum temperature, precipitation amount, mean sea-level pressure, mean station pressure, mean dew point, daily mean visibility, snow depth, and the occurrence of the following phenomena: fog, rain or drizzle, snow or ice pellets, hail, thunder, and

tornado/funnel clouds. The original records from all the weather stations have undergone extensive quality control procedures (more than 400 algorithms) by the Air Weather Service (see www.ncdc.noaa.gov/isd for details). These synoptic hourly observations were processed into mean daily values from recorded hourly data by the NCDC.

We focus our study on the decadal variation of *u* and other wind variables (maximum sustained wind speed, maximum wind gust) for the 40-year period of 1978-2017, when the data are the most complete. In selection of the final subset of stations in this study, we employ strict selection criteria to avoid including incomplete data series. Firstly, we only select stations with complete data for all the 40 years of the analysis (1978-2017), each year with complete records for all the 12 months. Secondly, each monthly value has to be derived from at least 15 days of data. Finally, the daily values have to be derived from a minimum of four observations. As a result, only 1,435 stations are included for analysis (locations of those stations are shown as red dots in Supplementary Fig. 3; and the mean number of observations in a day is shown in Supplementary Fig. 10; code and the processed data is available in Supplementary Data 1). Among them, 543 stations are automatic monitoring stations that are in operation during the entire study period. For some analyses (Supplementary Fig. 7) we relax our selection criteria to include more stations – for instance, by allowing 1, 5, 10 or 20 years of missing data. Last, the results show no dependence on whether global mean annual *u* or global median annual *u* is used to describe the decadal variation of global *u* (Supplementary Fig. 21 versus Fig. 1a).

We also repeat the wind analyses using the HadISD (version v2.0.2.2017f)[19] global sub-daily database, which is distributed by the Met Office Centre and is freely assessed from:

https://www.metoffice.gov.uk/hadobs/hadisd/. The dataset spans from 1931 to the end of 2017. The total number of stations in HadISD is 8,103, all of which passed quality control tests that are designed to remove bad data while keeping the extremes of wind speed and direction, temperature, dew point temperature, sea-level pressure, and cloud data (total, low, mid and high level). For example, quality control procedures have been performed on the major climatological variables, including a duplicate check, an isolated odd cluster check, a frequent values check, a distributional gap check, a world record check, a streak check, a climatological check, a spike check, a temperature-humidity cross check, a cloud-logical cross check, an excess variance check, and a neighbor outlier check[19]. In our analysis, we use the criteria as that described above to select stations that have uninterrupted, continuous monthly records during the period 1978-2017 (n = 1,542; code and the processed data is available in Supplementary Data 2).

Climate indices. The dynamics of ocean/atmospheric circulations can be described with climate indices. Almost all climate indices are associated with regional surface temperature anomalies (or temperature heterogeneity) to some extent, in particular sea surface temperature (SST). The anomaly in SST has a profound impact on the climate over land through the tight linkage between the oceans and the atmosphere[23,40,41]. The oceans, in particular in regions around the equator, act as a massive heat-retaining solar panel providing fundamental energy for the atmospheric engine to transfer the heat from the tropics to the poles through global circulation systems (i.e., Hadley, Ferrel, and polar cells) that have a profound impact on the global climate[40,42]. Even an apparently small change of SST in just one region can produce major climate variations over large areas of the planet[41]. For example, tropical Pacific cooling is found to be the cause of the recent ongoing

warming hiatus[23,43]. In general, regional variations in SST can trigger decadal variations in the climate indices, leading to decadal variations in the Earth's climate system[23,27,44].

We select 21 time series of climate indices describing monthly atmospheric and oceanic phenomena to compare decadal variations of the Earth's climate system with changes in wind speed (Supplementary Table 2). Only indices that are available for the whole study period (1978-2017) are considered (download from https://www.esrl.noaa.gov/psd/data/climateindices/list/). For example, we include the following eight teleconnection indices: Pacific Decadal Oscillation (PDO); Pacific North American Index (PNA); Western Pacific Index (WP); North Atlantic Oscillation (NAO); East Pacific/North Pacific Oscillation (EP/NP); North Pacific pattern (NP); East Atlantic pattern (EA); and Scandinavia pattern (SCAND). We include one atmospheric index (Arctic Oscillation (AO)) and one multivariate El Niño–Southern Oscillation (ENSO) index. We include six indices describing regional SST in Pacific oceans: Eastern Tropical Pacific SST (5°N – 5°S, 150° W – 90 °W) (NINO3); Central Tropical Pacific SST (5°N-5°S) (160°E-150°W) (NINO4); Extreme Eastern Tropical Pacific SST (0 – 10°S, 90°W – 80°W) (NINO12); East Central Tropical Pacific SST (5°N – 5°S) (170°W – 120°W) (NINO34); Oceanic Nino Index (ONI); and Western Hemisphere warm pool (WHWP). Two of the indices describe regional SST in Atlantic oceans—the Tropical Northern Atlantic Index (TNA) and the Tropical Southern Atlantic Index (TSA). The final three indices are the Atlantic Meridional Mode (AMM), the Southern Oscillation Index (SOI), and the 10.7-cm Solar Flux (Solar).

Statistical analyses. It is apparent that the trend varies in the time series of global and/or regional average mean annual *u* for different ranges of year (e.g., Fig. 1a). Traditional single linear model

443 does not provide an adequate description of a change in the tendency. In this study, we apply a
444 piecewise linear regression model[14,15] to quantify potential turning points in a given time series.
445 Piecewise linear regression is capable of detecting where the slope of a linear function changes,
446 and allows multiple linear models to be fitted to each distinct section of the time series. For a time
447 series y (e.g. global average mean annual *u*), a continuous piecewise linear regression model with
448 one turning point (TP) can be described as:

449 $$y = \begin{cases} \beta_0 + \beta_1 t + \varepsilon, & t \le TP \\ \beta_0 + \beta_1 t + \beta_2 (t - TP) + \varepsilon, & t > TP \end{cases} \quad (3)$$

450 where t is year; β_0 , β_1 and β_2 are regression coefficients; ε is the residual of the regression.
451 The linear trend is β_1 before the TP (year), and $\beta_1 + \beta_2$ after the TP. We use least square error
452 techniques to fit the model to the data and determine TP, β_0 , β_1 and β_2 . To avoid linear
453 regression in a period with too few years, we confine TP to be within the period of 1980 to 2015.
454 The necessity of introducing TP is tested statistically with the *t*-test under the null hypothesis that
455 " β_2 is not different from zero". The diagnostic statistics for the regression also include the
456 goodness of fit (R^2), the P value for the whole model, and the P values for the trends before and
457 after TP. We consider $P < 0.05$ as significant.
458
459 In addition, we use a forward stepwise regression algorithm[26] to select major climate indices that
460 have the largest explanatory power for the decadal variations in *u*. The algorithm is a systematic
461 method for adding predictors from a multilinear model according to their statistical significance in
462 explaining the response (decadal variation of *u* in this study). The initial regression model contains
463 only an intercept term. Then, the explanatory power of incrementally larger and smaller models is
464 compared to determine which predictor should be included. At each step, the P-value of an F-

statistic is calculated to examine models with a potential predictor that is not already in the model. The null hypothesis is that the predictor would have a zero coefficient if included in the model. If there is sufficient evidence at a given significant level to reject the null hypothesis, the predictor is added to the model. Therefore, the earlier the predictor enters in to the model, the larger the explanatory power the predictor has.

Analyses on the possible causes for the decadal variation in wind speed. Overall, the twenty-one climate indices explain 90% of the multi-decadal scale, year-to-year variation in global mean annual *u* (adjusted R^2 = 78%). Regionally, they explain 91%, 75% and 87% of the multi-decadal scale, year-to-year variation in mean annual *u* for North America (adjusted R^2 = 81%), Europe (adjusted R^2 = 46%) and Asia (adjusted R^2 = 71%), respectively. Globally, the indicators significantly correlated with *u* include TNA (R = -0.50; P-value < 0.01), PDO (R = 0.46; P < 0.01), WHWP (R = -0.46; P < 0.01), NAO (R = 0.39; P < 0.05), AMM (R = -0.39; P < 0.05), EP/NP (R = 0.37; P < 0.05), TSA (R = -0.38; P < 0.05), Solar (R = 0.35; P < 0.05), SOI (R = -0.32; P < 0.05), and EA (R = 0.31; P < 0.05). All the significant indicators are determined from the SST anomaly over some regions of the tropics, except NAO and EA which are closely relevant to the Arctic oscillation. Among these indicators, TNA is the most significant indicator for *u* change over North America (R = -0.63; P < 0.01); NAO is the most significant indicator for Europe (R = 0.37; P < 0.05); and PDO for Asia (R = 0.50; P < 0.01) (Supplementary Table 2).

According to the forward stepwise regression analysis, as for global mean annual *u*, the first six climate indices include in the model are TNA, PDO, AMM, Solar, WHWP, and SCAND (Supplementary Table 3). Regionally, similar to the correlation analysis, TNA has the largest

explanatory power for *u* over North America; NAO has the largest explanatory power for *u* over Europe; and PDO has the largest explanatory power for *u* over Asia (Supplementary Table 3). Furthermore, we randomly select 40% of stations for the calculation of global/regional *u* and repeat the analyses for 300 times to estimate the uncertainty (number in parentheses in Supplementary Table 3 shows how many times climate indices are selected as six major predictors). Last, the six climate indices explain 70 ±5%, 79 ±3%, 48 ±9%, and 51 ±8% of the multi-decadal scale, year-to-year variation in mean annual *u* for the globe, North America, Europe, and Asia, respectively (Supplementary Table 3, Supplementary Fig. 15).

Calculations for wind power assessments. Due to the nonlinear relationship between wind power (P) and wind speed (*u*) (Equation (1)), high temporal resolution data are needed for *u* to produce an accurate estimate of P. Thus, we use the HadISD global sub-daily database from the Met Office Centre[19]. For each station that has uninterrupted, continuous monthly records during the period 1978-2017 (n = 1,542), we use linear interpolation to interpolate a sub-daily time series to an hourly time series. Fig. 4a shows the frequency distributions of global average hourly wind speed in 2010 and 2017, and the year 2024, assuming the same increasing rate.

We then discuss annual wind power production given these wind speed time series (2010, 2017 and 2024), considering that production is dependent on the specifications of wind turbines. Here we use General Electric GE 2.5 – 120 (ref. 31) as an example. The parameters for this turbine include the following: rated power, 2,500.0 kW; cut-in wind speed, 3.0 m s^{-1}; cut-out wind speed, 25.0 m s^{-1}; diameter, 120 m; swept area, 11,309.7 m^2; and hub height: 110/139 m (here we take 120 m). The power curve for this turbine is shown in Supplementary Fig. 22. The wind speed time

series (2010, 2017 and 2024) at the height of the turbine (i.e. 120 m) are first estimated using the wind profile power law (Equation (2)), and are then converted into the hourly wind power (Supplementary Fig. 19) using the power curve (Supplementary Fig. 22). Owing to the increase frequency of high u, annual wind power production from the turbine increases from 2.4 million kWh in 2010 to 2.8 million kWh in 2017; and to 3.3 million kWh in 2024. As a result, the overall capacity factor increases 1.9% during 2010-2017, and 2.2% during 2018-2024.

To compare the significance of the increased capacity factor induced by the strengthening u with that due to technology innovation (e.g. improvement of the turbine's power efficiency), we collect the overall capacity factor for wind generation in the U.S. from the U.S. Energy Information Administration[32] (the black line in Fig. 4b). In the U.S., the overall capacity factor is highly correlated with the cube of regional wind speed (u^3) ($R = 0.86$, $P < 0.01$; Fig. 4b). Even for the detrended time series, the correlation coefficient between capacity factor and u^3 is as high as 0.71 ($P < 0.05$), showing that wind speed is a key factor for the year-to-year variation of wind power energy production. It is well known that technology innovation is a key factor that drives the increase of capacity factor for wind generation[33]. To isolate the u-induced increase in capacity factor from that due to technology innovation, we use the regional mean hourly wind speed in 2010, 2017 and 2024 (assuming the same increasing rate) to estimate the increase of capacity factor for a given turbine, thereby controlling for technology innovation. The u-induced increase in capacity factor is +2.5% between 2010 and 2017, and +3.2% between 2017 and 2024. It explains more than 50% of the overall increase of capacity factor for wind generation in the United States.

We also collect information of the installed turbines from the U.S. Wind Turbine Database (n = 57,646; https://eerscmap.usgs.gov/uswtdb) (locations refer to Supplementary Fig. 23). The turbine with the nearest distance to one of the HadISD weather stations (n = 1,542) is at Deaf Smith County, the U.S. (<1 km; wind farm name: Hereford 1; case ID: 3047384; location see the inset plot in Fig. 4c). The turbine was installed in 2014. The turbine is a General Electric GE 1.85 – 87 (ref. 34). The parameters for this turbine include: rated power, 1,850.0 kW; cut-in wind speed, 3.0 m s^{-1}; rated wind speed, 12.5 m s^{-1}; cut-out wind speed, 25.0 m s^{-1}; diameter, 87.0 m; swept area, 5,945.0 m^2; hub height: 80 m. We combine these parameters with Equation (1) to estimate the power curve for the turbine (Supplementary Fig. 24). Finally, we integrate the power curve with the hourly wind speed from 1978 to 2017 at the hub height at this station to calculate annual wind power production generated by the General Electric GE 1.85 – 87 turbine (Supplementary Fig. 25a; red bars in Fig. 4d). In addition, we calculate annual wind power production at the station generated by the General Electric GE 2.5 – 120 turbine (Supplementary Fig. 25b; green bars in Fig. 4d). We also use the Equation (1) to estimate maximum annual wind power production at the station given diameter of 120 m and hub height of 120 m (the same as the General Electric GE 2.5 – 120 turbine), which is constrained by the Betz Limit (f = 16/27 in Equation (1)) (Supplementary Fig. 25c; blue bars in Fig. 4d). The Beltz Limit describes the theoretical maximum ratio of power that can be extracted by a wind turbine to the total power contained in the wind.

Data availability. The data for quantifying wind speed changes are the Global Surface Summary of the Day database (GSOD, ftp://ftp.ncdc.noaa.gov/pub/data/gsod), and the HadISD (version v2.0.2.2017f) global sub-daily database (https://www.metoffice.gov.uk/hadobs/hadisd/). The time series of climate indices describing monthly atmospheric and oceanic phenomena are obtained

from the National Oceanic and Atmospheric Administration (https://www.esrl.noaa.gov/psd/data/climateindices/list/). Simulated wind speed changes in Coupled Model Intercomparison Project Phase 5 (CMIP5) are available in the Program for Climate Model Diagnosis and Intercomparison (https://esgf-node.llnl.gov/projects/cmip5/). Simulated wind speed changes constrained by historical sea surface temperature are provided by the IPSL Dynamic Meteorology Laboratory. Wind records in reanalysis products include the ECMWF ERA-Interim Product (apps.ecmwf.int/datasets/data/interim-full-daily/) and the NCEP/NCAR Global Reanalysis Product (http://rda.ucar.edu/datasets/ds090.0/). The processed wind records and the relevant code are available in Supplementary Data 1 and 2. All datasets are also available on request from Z. Zeng.

Code availability. The program used to generate all the results is MATLAB (R2014a) and ArcGIS (10.4). Analysis scripts are available by request from Z. Zeng. The code producing wind records are available in Supplementary Data 1 and 2.

References.

1. Roderick, M. L., Rotstayn, L. D., Farquhar, G. D. & Hobbins, M. T. On the attribution of changing pan evaporation. *Geophys. Res. Lett.* **34,** 1–6 (2007).

2. Vautard, R., Cattiaux, J., Yiou, P., Thépaut, J. N. & Ciais, P. Northern Hemisphere atmospheric stilling partly attributed to an increase in surface roughness. *Nat. Geosci.* **3,** 756–761 (2010).

3. Mcvicar, T. R., Roderick, M. L., Donohue, R. J. & Van Niel, T. G. Less bluster ahead? ecohydrological implications of global trends of terrestrial near-surface wind speeds. *Ecohydrology* **5,** 381–388 (2012).

4. McVicar, T. R. *et al.* Global review and synthesis of trends in observed terrestrial near-surface wind speeds: Implications for evaporation. *J. Hydrol.* **416–417,** 182–205 (2012).

5. Tian, Q., Huang, G., Hu, K., & Niyogi, D. Observed and global climate model based changes in wind power potential over the Northern Hemisphere during 1979–2016. *Energy* doi: https://doi.org/10.1016/j.energy.2018.11.027iyo (2018).

6. Lu, X., McElroy, M. B. & Kiviluoma, J. Global potential for wind-generated electricity. *Proc. Natl. Acad. Sci.* **106,** 10933–10938 (2009).

7. Zhu, Z. *et al.* Greening of the Earth and its drivers. *Nat. Clim. Chang.* **6,** 791–796 (2016).

8. Torralba, V., Doblas-Reyes, F. J. & Gonzalez-Reviriego, N. Uncertainty in recent near-surface wind speed trends: a global reanalysis intercomparison. *Environ. Res. Lett.* **12,** 114019 (2017).

9. UNFCCC. *Adoption of the Paris Agreement* (FCCC/CP/2015/L.9/Rev.1., 2015).

10. IPCC. *Summary for policymakers in Climate change 2014: Mitigation of climate change. Contribution of working group III to the fifth assessment report of the Intergovernmental Panel on Climate Change* (O. Edenhofer et al., Eds., Cambridge University Press, Cambridge, UK and New York, USA, 2014).

11. U.S. Department of Energy. *Projected growth wind industry now until 2050* (Washington, D.C., 2018).

12. Nathan, R. & Muller-landau, H. C. Spatial patterns of seed dispersal, their determinants and consequences for recruitment. *Trends Ecol. Evol.* **15,** 278–285 (2000).

13. Global Wind Energy Council. *Global Wind Energy Outlook 2018* (2018).

14. Toms, J. D. & Lesperance, M. L. Piecewise regression: a tool for identifying ecological thresholds. *Ecology* **84,** 2034–2041 (2003).

15. Ryan, S. E. & Porth, L. S. *A tutorial on the piecewise regression approach applied to bedload transport data* (2007).

16. Azorin-Molina, C. *et al.* Homogenization and assessment of observed near-surface wind speed trends over Spain and Portugal, 1961-2011. *J. Clim.* **27,** 3692–3712 (2014).

17. Kim, J. C. & Paik, K. Recent recovery of surface wind speed after decadal decrease: a focus on South Korea. *Clim. Dyn.* **45,** 1699–1712 (2015).

18. Azorin-Molina, C., Dunn, R. J. H., Mears, C. A., Berrisford, P. & McVicr, T. R. 2018: [Global climate; Atmospheric circulation] Surface winds [in "State of the Climate in 2017"]. *Bull. Am. Meteorol. Soc.* **99,** S41-S43, doi: 10.1175/2018BAMSStateoftheClimate (2018).

19. Dunn, R. J. H., Willett, K. M., Morice, C. P. & Parker, D. E. Pairwise homogeneity assessment of HadISD. *Clim. Past* **10,** 1501–1522 (2014).

20. Zeng, Z. *et al.* Global terrestrial stilling: does Earth's greening play a role? *Environ. Res. Lett.* Accepted (2018).

21. Held, I. M., Ting, M. & Wang, H. Northern winter stationary waves: Theory and modeling. *J. Clim.* **15,** 2125–2144 (2002).

22. Hurrell, J. W., Kushnir, Y., Ottersen, G. & Visbeck, M. *The North Atlantic Oscillation climatic*

significance and environmental impact (eds. Hurrell, J. W., Kushnir, Y., Ottersen, G. & Visbeck, M., 2003).

23. Kosaka, Y. & Xie, S. P. Recent global-warming hiatus tied to equatorial Pacific surface cooling. *Nature* **501,** 403–407 (2013).

24. Wang, C. Z. Atlantic climate variability and its associated atmospheric circulation cells. *J. Clim.* **15,** 1516–1536 (2002).

25. Zhang, Y., Xie, S.-P., Kosaka, Y. & Yang, J.-C. Pacific Decadal Oscillation: Tropical Pacific Forcing versus Internal Variability. *J. Clim.* **31,** 8265–8279 (2018).

26. Draper, N. R. & Smith, H. *Applied Regression Analysis, 3rd Edition* (Wiley-Interscience, 1998).

27. Timmermann, A. *et al.* El Niño-Southern Oscillation complexity. *Nature* **559,** 535–545 (2018).

28. Archer, C. L. Evaluation of global wind power. *J. Geophys. Res.* **110,** D12110 (2005).

29. Elliott, D. L., Holladay, C. G., Barchet, W. R., Foote, H. P. & Sandusky, W. F. *Wind Energy Resource Atlas of the United States* (1986).

30. Peterson, E. W. & Hennessey, J. P. On the use of power laws for estimates of wind power potential. *Journal of Applied Meteorology* **17,** 390–394 (1978).

31. Wind-turbine-models.com. General Electric GE 2.5 - 120. (2018). at <https://www.en.wind-turbine-models.com/turbines/310-general-electric-ge-2.5-120>

32. U.S. Energy Information Administration. Capacity Factors for Utility Scale Generators Not Primarily Using Fossil Fuels, January 2013-August 2018. (2018). at <https://www.eia.gov/electricity/monthly/epm_table_grapher.php?t=epmt_6_07_b>

33. Dell, J. & Klippenstein, M. Wind Power Could Blow Past Hydro's Capacity Factor by 2020. (2018). at <https://www.greentechmedia.com/articles/read/wind-power-could-blow-past-hydros-

capacity-factor-by-2020>

34. Wind-turbine-models.com. General Electric GE 1.85 - 87. (2018). at https://www.en.wind-turbine-models.com/turbines/745-general-electric-ge-1.85-87

35. Steinman, B. A. *et al.* Atlantic and Pacific multidecadal oscillations and Northern Hemisphere temperatures. *Science* **347,** 988-991(2015).

36. Hughes, G. *The Performance of Wind Farms in the United Kingdom and Denmark* (the Renewable Energy Foundation, 2012).

37. Morice, C. P., Kennedy, J. J., Rayner, N. A. & Jones, P. D. Quantifying uncertainties in global and regional temperature change using an ensemble of observational estimates: The HadCRUT4 data set. *J. Geophys. Res. Atmos.* **117,** 1–22 (2012).

38. Reynolds, R. W., Rayner, N. A., Smith, T. M., Stokes, D. C. & Wang, W. An improved in situ and satellite SST analysis for climate. *J. Clim.* **15,** 1609–1625 (2002).

39. WMO Resolution 40 (Cg-XII). *Exchanging meteorological data: Guidelines on relationships in commercial meteorological Aativities: WMO policy and practice* (WMO, 1996).

40. Wallace, J. & Hobbs, P. *Atmospheric science: an introductory survey* (Academic Press, 2006).

41. News, O. S. & Atlantic, N. Surface warming hiatus caused by increased heat uptake across multiple ocean basins. *Geophys. Res. Lett.* **41,** 7868–7874 (2014).

42. Makarieva, A. M., Gorshkov, V. G., Sheil, D., Nobre, A. D. & Li, B. L. Where do winds come from? A new theory on how water vapor condensation influences atmospheric pressure and dynamics. *Atmos. Chem. Phys.* **13,** 1039–1056 (2013).

43. England, M. H. *et al.* Recent intensification of wind-driven circulation in the Pacific and the ongoing warming hiatus. *Nat. Clim. Chang.* **4,** 222–227 (2014).

44. Chang, P., Ji, L. & Li, H. A decadal climate variation in the tropical Atlantic Ocean from

662 thermodynamic air-sea interactions. *Nature* **385,** 516 (1997).
663 45. European Centre for Medium-Range Weather Forecasts, ERA-Interim Project,
664 https://doi.org/10.5065/D6CR5RD9, Research Data Archive at the National Center for
665 Atmospheric Research, Computational and Information Systems Laboratory, Boulder, Colo.
666 (Updated monthly.) Accessed 10 AUG 2018.
667 46. National Centers for Environmental Prediction/National Weather Service/NOAA/U.S.
668 Department of Commerce, NCEP/NCAR Global Reanalysis Products, 1948-continuing,
669 http://rda.ucar.edu/datasets/ds090.0/, Research Data Archive at the National Center for
670 Atmospheric Research, Computational and Information Systems Laboratory, Boulder, Colo.
671 (Updated monthly.) Accessed 10 AUG 2018.
672 47. Zhu, Z. *et al.* Global data sets of vegetation leaf area index (LAI)3g and fraction of
673 photosynthetically active radiation (FPAR)3g derived from global inventory modeling and
674 mapping studies (GIMMS) normalized difference vegetation index (NDVI3G) for the period 1981
675 to 2011. *Remote Sens.* **5,** 927–948 (2013).
676 48. Liu, X. *et al.* High-resolution multi-temporal mapping of global urban land using Landsat
677 images based on the Google Earth Engine Platform. *Remote Sens. Environ.* **209,** 227–239 (2018).
678 Pettitt AN. 1979. A non-parametric approach to the change-point problem. J. R. Stat. Soc. Ser. C:
679 Appl. Stat. 28(2): 126–135. https://doi.org/10.2307/2346729.
680 Copernicus Climate Change Service (C3S) (2017): ERA5: Fifth generation of ECMWF
681 atmospheric reanalyses of the global climate . Copernicus Climate Change Service Climate Data
682 Store (CDS), date of access. https://cds.climate.copernicus.eu/cdsapp#!/home
683 Tsonis, A. A., et al. (2007). "A new dynamical mechanism for major climate shifts." Geophysical
684 Research Letters 34(13): n/a-n/a.

Henriksson, S. V. (2018). "Interannual oscillations and sudden shifts in observed and modeled climate." Atmospheric Science Letters 19(10): e850.

Wu, J., Zha, J. L., Zhao, D. M., & Yang, Q. D. Changes in terrestrial near-surface wind speed and their possible causes: an overview. Climate Dynamics 51, 2039-2078 (2018).

Granger, C.W.J., 1969. "Investigating causal relations by econometric models and cross-spectral methods". Econometrica 37 (3), 424–438.

Pryor SC, Barthelmie RJ, Young DT, Takle ES, Arritt RW, Flory D, Gutowski WJ Jr, Nunes A, Roads J. 2009. Wind speed trends over the contiguous USA. Journal of Geophysical Research - Atmospheres 114: D14105, DOI: 10.1029/2008JD011416

Additional information

Supplementary information is available in the online version of the paper. Reprints and permissions information is available online at www.nature.com/reprints.

Correspondence and requests for materials should be addressed to Z. Zeng.

Acknowledgements

This study was supported by Lamsam-Thailand Sustain Development (B0891). J. Liu was supported by the National Natural Science Foundation of China (41625001). We thank Della Research Computing in Princeton University for providing computing resources. We thank the USA? National Climatic Data Center and the UK Met Office Centre for providing surface wind speed measurements, and thank the Program for Climate Model Diagnosis and Intercomparison and the IPSL Dynamic Meteorology Laboratory for providing surface wind speed simulations.

Author contributions

Z. Zeng and E. Wood designed the research. Z. Zeng and L. Yang performed analysis; Z. Zeng, A. Ziegler, T. Searchinger wrote the draft; and all the authors contributed to the interpretation of the results and the writing of the paper.

Competing financial interests

The authors declare no competing financial interests.

718 **Figure Legends.**

719 **Figure 1. Turning point for mean global surface wind speed (*u*).** (**a**) Global mean annual *u*
720 during 1978-2017 (black dot and line). The piecewise linear regression model indicates a
721 statistically significant turning point in 2010. The red line is the piecewise linear fit (R^2 = 90%, P
722 < 0.001). The dashed line indicates the turning point. The trends before and after the turning point
723 are shown in the inset. Each grey line (n = 300) is a piecewise linear fit for a randomly selected
724 subset (40%) of the global stations. (**b**) Frequency distribution of the estimated turning points
725 derived from the 300 resampling results. (**c**) Frequency distribution of the trends in mean annual
726 *u* before and after the turning point from the 300 resampling results. The result is grounded on the
727 weather stations in the GSOD database.

728 **Figure 2. Factors driving the decadal variations in *u*.** Observed (red) and reconstructed (black)
729 detrended mean annual *u* over the following: (**a**) the globe, (**b**) North America, (**c**) Europe, and (**d**)
730 Asia. For the globe and each of the three continents, we select six largest explanatory climate
731 indices for the decadal variations of *u* with a stepwise forwarding regression model. The selected
732 climate indices are then used to reconstruct decadal variations of *u* via a multiple regression.
733 Uncertainties are the inter-quartile range of the results based on a randomly selected 40% subset
734 of the station pools (repeated 300 times). Inset plots indicate the locations of the stations. The
735 models are trained only using the detrended time series before the turning points. The dashed line
736 indicates the turning point (2010 for the globe, 2012 for North America, 2003 for Europe, and
737 2001 for Asia). Inset black numbers are coefficients of determination between observed and

reconstructed *u* before the turning points. Inset red numbers are correlation coefficient and its significance between observed and reconstructed *u* after the turning points.

Figure 3. Mechanisms for the decadal variation in *u*. Normalized mean annual surface temperature for the years with negative (**a**) and positive (**b**) anomalies of detrended wind. Characteristic regions for Pacific Decadal Oscillation (PDO), North Atlantic Oscillation (NAO) and Tropical Northern Atlantic Index (TNA) are outlined by green, red, and blue boxes, respectively. Surface temperature over land is obtained from Climate Research Unit TEM4 with a spatial resolution of 5° by 5° (ref. 37), and that over ocean is from NOAA Optimum Interpolation (OI) Sea Surface Temperature V2, with a spatial resolution of 1° by 1° (ref. 38). Spatial patterns of the correlation between the regional ($5^o \times 5^o$) mean annual *u* and the following: (**c**) TNA; (**d**) NAO; and (**e**) PDO for 1978-2017. Dotting represents significant at $P < 0.05$ level. Decadal variations are shown in panels (**f**) for TNA and regional *u* in North America; (**g**) for NAO and regional *u* in Europe; and (**h**) for PDO and regional *u* in Asia. The thin lines are annual values; and the thick lines are 9-year-window moving averages. The black lines are wind speed; and each of the colored lines are TNA, NAO, and PDO, respectively.

Figure 4. Implications of the recent reversal in global terrestrial stilling for wind energy industry. (**a**) Frequency distribution of global average hourly *u* in 2010 and 2017, and the year 2024 assuming the same increasing rate. (**b**) Time series of the overall capacity factor for wind generation in the U.S. (black line) and the three-order of the regional-average *u* (u^3; blue line) from 2008 to 2017. The inset scatter plot shows the significant relationship between the overall capacity factor and the regional u^3 ($R = 0.86$, $P < 0.01$). The inset black numbers show the trend in the overall capacity factor for wind generation, and the inset red numbers show the *u*-induced increase of capacity factor in the USA. (**c**) Mean annual *u* observed at a weather station near an installed

761 turbine at Deaf Smith County, USA. (<1 km). The inset plot shows the location. The turbine was
762 installed in 2014. The background colors separate different periods: P0, the 1980s level when *u* is
763 relative strong (1978-1995); P1, the evaluation years before the installation of the turbine (2009-
764 2013); P2, the operation years when the turbine is generating power (2014-2017). (**d**) Mean annual
765 wind power production at Deaf Smith County, the U.S. from different wind turbines during
766 different periods (red: General Electric GE 1.85 – 87; green: General Electric GE 2.5 – 120 turbine;
767 blue: the theoretical maximum ratio of power that can be extracted by a wind turbine given
768 diameter of 120 m and hub height of 120 m). Error bars show the interannual variability within the
769 periods.
770
771

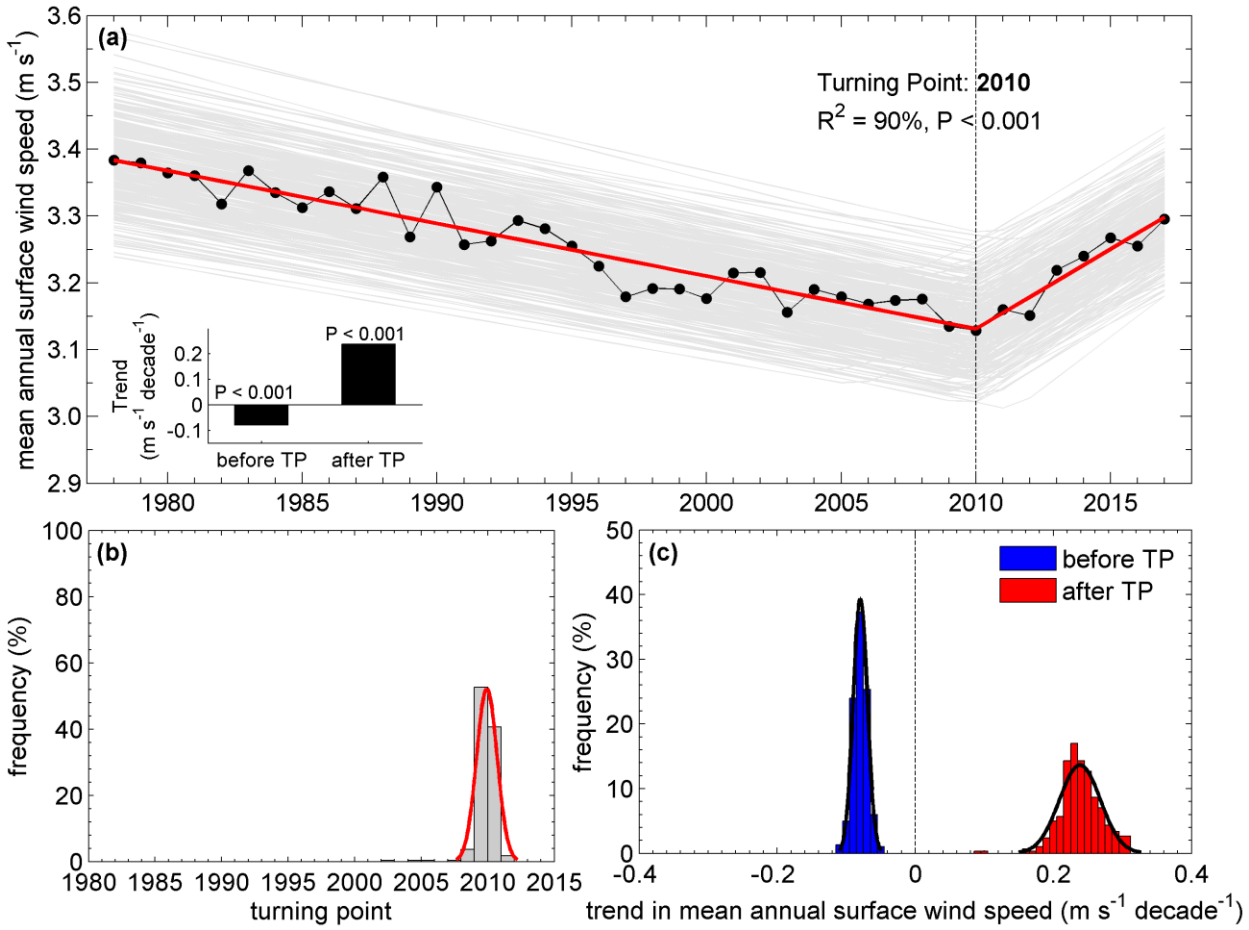

Figure 1. Turning point for mean global surface wind speed (*u*). (**a**) Global mean annual *u* during 1978-2017 (black dot and line). The piecewise linear regression model indicates a statistically significant turning point in 2010. The red line is the piecewise linear fit (R^2 = 90%, P < 0.001). The dashed line indicates the turning point. The trends before and after the turning point are shown in the inset. Each grey line (n = 300) is a piecewise linear fit for a randomly selected subset (40%) of the global stations. (**b**) Frequency distribution of the estimated turning points derived from the 300 resampling results. (**c**) Frequency distribution of the trends in mean annual *u* before and after the turning point from the 300 resampling results. The result is based on the weather stations in the GSOD database.

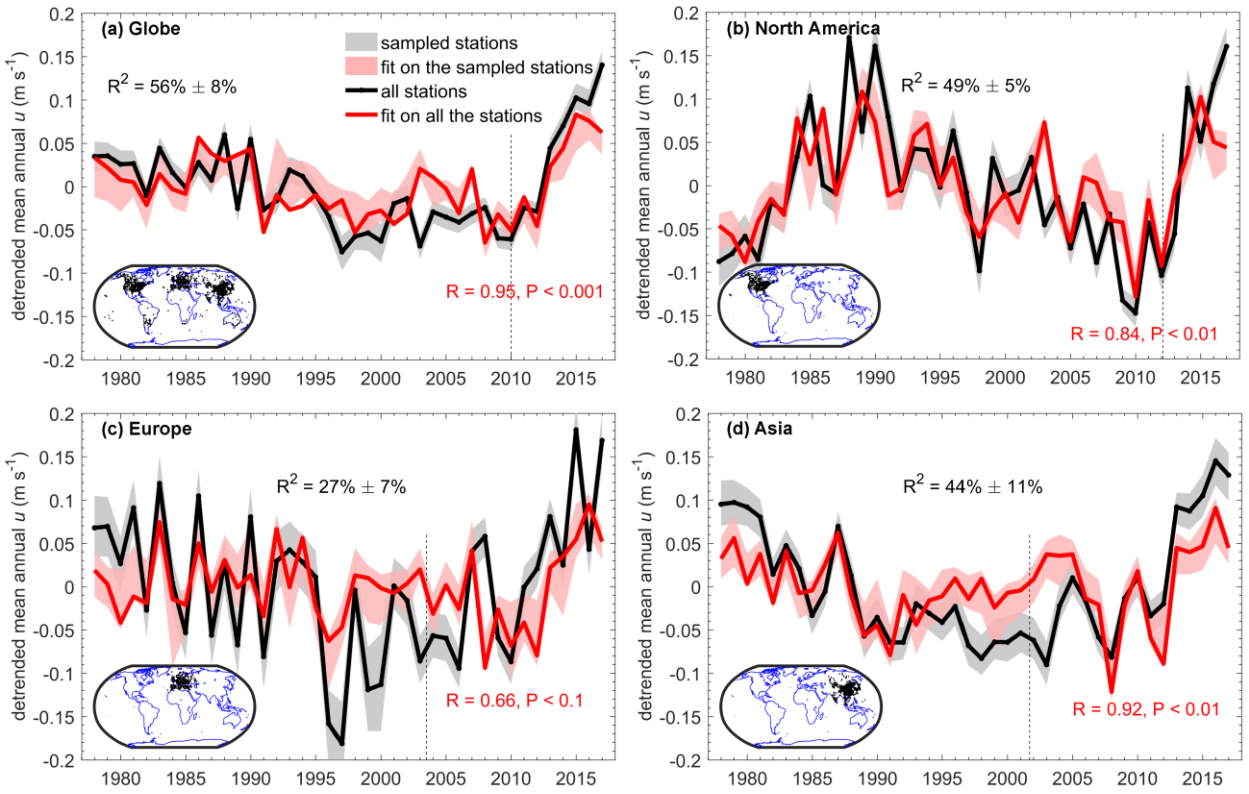

783 **Figure 2. Factors driving the decadal variations in *u*.** Observed (red) and reconstructed (black)
784 detrended mean annual *u* over the following: (**a**) the globe, (**b**) North America, (**c**) Europe, and (**d**)
785 Asia. For the globe and each of the three continents, we select six largest explanatory climate
786 indices for the decadal variations of *u* with a stepwise forwarding regression model. The selected
787 climate indices are then used to reconstruct decadal variations of *u* via a multiple regression.
788 Uncertainties are the inter-quartile range of the results based on a randomly selected 40% subset
789 of the station pools (repeated 300 times). Inset plots indicate the locations of the stations. The
790 models are trained only using the detrended time series before the turning points. The dashed line
791 indicates the turning point (2010 for the globe, 2012 for North America, 2003 for Europe, and
792 2001 for Asia). Inset black numbers are coefficients of determination between observed and

reconstructed *u* before the turning points. Inset red numbers are correlation coefficient and its significance between observed and reconstructed *u* after the turning points.

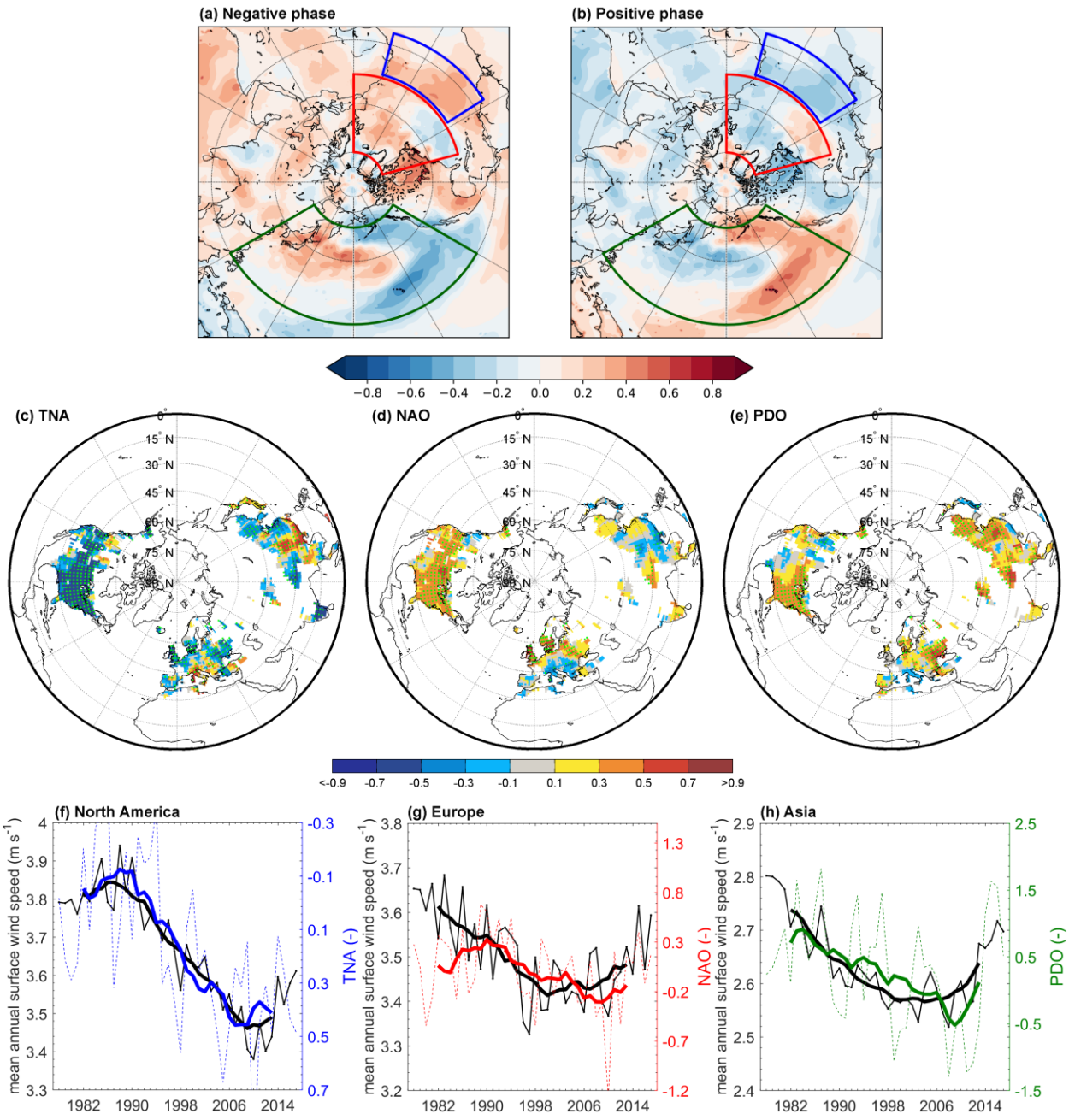

Figure 3. Mechanisms for the decadal variation in *u*. Normalized mean annual surface temperature for the years with negative (**a**) and positive (**b**) anomalies of detrended wind. Characteristic regions for Pacific Decadal Oscillation (PDO), North Atlantic Oscillation (NAO) and Tropical Northern Atlantic Index (TNA) are outlined by green, red, and blue boxes, respectively. Surface temperature over land is obtained from Climate Research Unit TEM4 with a

spatial resolution of 5° by 5° (ref. 37), and that over ocean is from NOAA Optimum Interpolation (OI) Sea Surface Temperature V2, with a spatial resolution of 1° by 1° (ref. 38). Spatial patterns of the correlation between the regional ($5^o \times 5^o$) mean annual *u* and the following: (**c**) TNA; (**d**) NAO; and (**e**) PDO for 1978-2017. Dotting represents significant at $P < 0.05$ level. Decadal variations are shown in panels (**f**) for TNA and regional *u* in North America; (**g**) for NAO and regional *u* in Europe; and (**h**) for PDO and regional *u* in Asia. The thin lines are annual values; and the thick lines are 9-year-window moving averages. The black lines are wind speed; and each of the colored lines are TNA, NAO, and PDO, respectively.

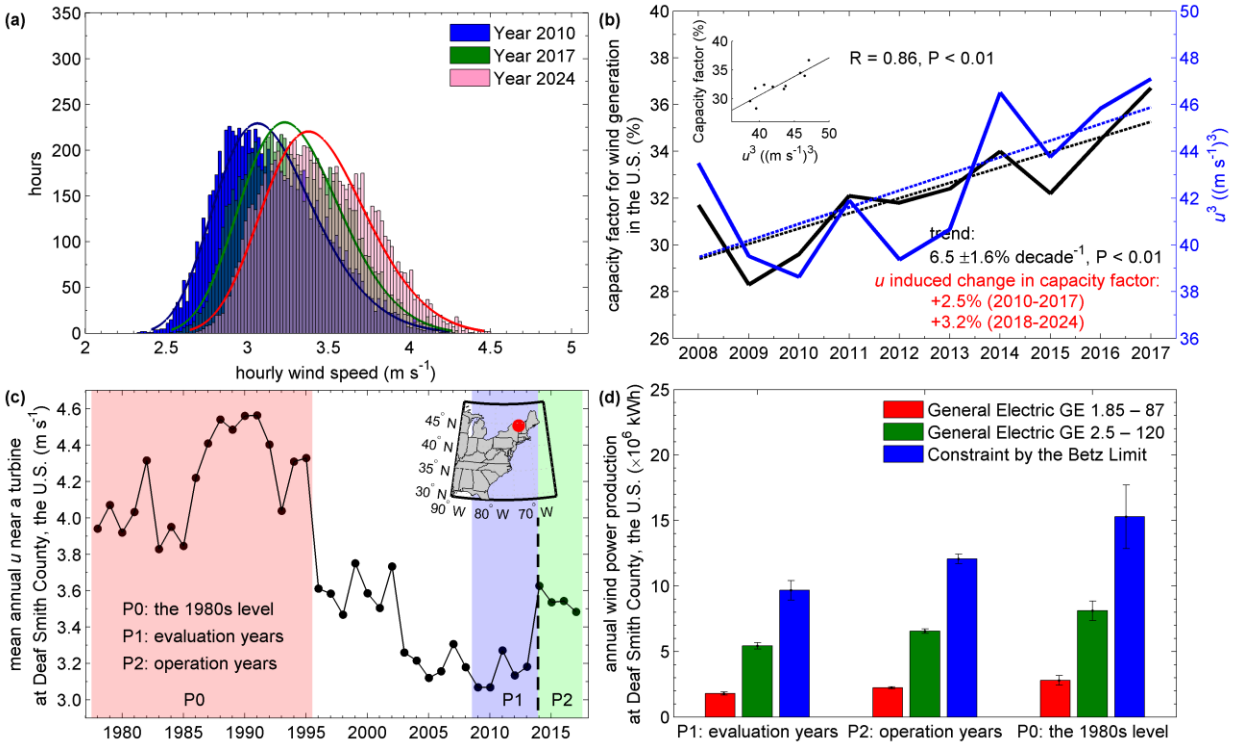

Figure 4. Implications of the recent reversal in global terrestrial stilling for wind energy industry. (**a**) Frequency distribution of global average hourly *u* in 2010 and 2017, and the year 2024 assuming the same increasing rate. (**b**) Time series of the overall capacity factor for wind generation in the U.S. (black line) and the three-order of the regional-average *u* (u^3; blue line) from 2008 to 2017. The inset scatter plot shows the significant relationship between the overall capacity factor and the regional u^3 (R = 0.86, P < 0.01). The inset black numbers show the trend in the overall capacity factor for wind generation, and the inset red numbers show the *u*-induced increase of capacity factor in the United States. (**c**) Mean annual *u* observed at a weather station near an installed turbine at Deaf Smith County, the U.S. (<1 km). The inset plot shows the location. The turbine was installed in 2014. The background colors separate different periods: P0, the 1980s level when *u* is relative strong (1978-1995); P1, the evaluation years before the installation of the turbine (2009-2013); P2, the operation years when the turbine is generating power (2014-2017). (**d**) Mean annual wind power production at Deaf Smith County, the U.S. from different wind

turbines during different periods (red: General Electric GE 1.85 – 87; green: General Electric GE 2.5 – 120 turbine; blue: the theoretical maximum ratio of power that can be extracted by a wind turbine given diameter of 120 m and hub height of 120 m). Error bars show the interannual variability within the periods.